Journal of The Electrochemical Society

OPEN ACCESS

Si Swarf Wrapped by Graphite Sheets for Li-Ion Battery Electrodes with Improved Overvoltage and Cyclability

To cite this article: Jaeyoung Choi *et al* 2021 *J. Electrochem. Soc.* **168** 020521

Journal of The Electrochemical Society, 2021 **168** 020521

Si Swarf Wrapped by Graphite Sheets for Li-Ion Battery Electrodes with Improved Overvoltage and Cyclability

Jaeyoung Choi, Jiasheng Wang, and Taketoshi Matsumoto[z]

The Institute of Scientific and Industrial Research, Osaka University, Ibaraki, Osaka 567-0047, Japan

Composites of flake-shaped Si nanopowder from swarf treated as an industrial waste and ultrathin graphite sheets (GSs) (Si:C = 5:1 wt) are used in Li-ion battery electrodes. Si nanopowder is dispersed and wrapped between GSs fabricated from expanded graphite. The delithiation capacity of the Si/GS composite electrode during 300 cycles is 1.69 ~ 0.83 mAh cm^{-2} (0.5 C), while that of the electrode with C-coated Si nanopowder (Si:C = 10:1 wt) fabricated in C_2H_4 is 1.55 ~ 0.72 mAh cm^{-2}. The series resistances (R_s) for the Si/GS electrode are a half and two-thirds of those for the C-coated Si electrode at the 6th and 300th cycles, respectively. The charge transfer resistance (R_{ct}) for the Si/GS electrode is two-thirds of that for the C-coated Si electrode at the 300th cycle. GS bridges are formed across cracks, and suppress cracking and peeling-off of Si. Agglomerated GSs wrap Si/GS composites, and work as stable frameworks that secure electrolyte paths and buffer spaces for Si volume change. In the C-coated Si electrodes, Si frameworks fuse after the 300th cycle, leading to low delithiation capacities. The delithiation capacity of 4 mAh cm^{-2} for more than 75 cycles is achieved by the Si/GS electrode at the current density of 5 mA cm^{-2} with delithiation limitation at 1200 mAh g^{-1}.

 [DOI: 10.1149/1945-7111/abdd7e]

Manuscript submitted July 13, 2020; revised manuscript received January 4, 2021. Published February 8, 2021.

Supplementary material for this article is available online

Li-ion batteries (LIBs) are widely used in various mobile electronics. Concerns of global warming and climate change have recently boosted the demand of LIBs for electric vehicles and solar photovoltaic output smoothing. Si has been studied as an active material with a high theoretical capacity of 3578 mAh g^{-1}, which is around ten times higher than that of graphite (372 mAh g^{-1}).[1,2] Si nanopowder smaller than 150 nm was reported to suppress peeling-off of Si caused by the large volume change during lithiation/delithiation cycles.[3] Miniaturization of Si also moderates the degradation of the cell performance due to the low ionic conductivity and electrical conductivity of Si.[4,5] We have investigated the reaction mechanisms of Si swarf electrodes.[6–8] Si swarf is a flake-shaped nano-Si material generated with nearly half the weight of a Si ingot for solar cells during the slicing process. 0.1 million tons of Si swarf are generated per year over the world from Si ingots that are produced with processes at 1000 °C ~ 1800 °C from silica. Si swarf is generally treated as an industrial waste. Water-based coolant and the fixed abrasive grain wire saws are paving the way to the use of Si swarf as an anode active material with a high capacity at a reduced cost.

Nano carbon materials have been added in Si electrodes to improve the electrical conductivity and the cyclability because large graphite powder affords Si nanopowder at less than 10 wt%.[9] A carbon layer deposited on Si nanopowder under C_2H_2, C_2H_4 or CH_4 atmosphere at 800 °C ~ 1000 °C with or without CO_2 showed better cyclabilities.[6–8,10,11] The wrinkle structure composed of Si frames partly covered by a C layer showed mechanical stability after the 100th lithiation/delithiation cycles. Graphene is an attractive material fabricated on a Cu foil at 1000 °C,[12] but a production method at a reduced cost is desired. Graphene oxide fabricated by oxidation such as the Hummer's method is relatively small, the electrical conductivity was imperfectly recovered by the post reduction due to remained defects,[13–16] and organic compounds such as binders and thiophene were carbonized to cover the defects by heating at 800 °C ~ 900 °C under inert gas atmosphere.[13,17] Few layer graphene (FLG) was used with micron-sized silicon particles [18] and binders.[19] Many strategies for dealing with large volume change of Si electrodes at relatively high costs such as yolk-shell structures,[20,21] Ni foam,[22] Si nanotubes,[23] mixtures with carbon nanotubes,[24,25] and coating Si with polyaniline and polypyrrole[26] have been demonstrated. SiO[25] is used commercially to reduce the volume change of the electrode at the sacrifice of the capacity. However, the Si electrodes do not combine all requirements of a high electrode performance, a reduced cost, environmental friendliness of materials and processes, and circular economy.

In this study, Si/graphite sheet (GS) composites from Si swarf and expanded graphite are used as the active material with a reduced cost and thermal budget. Ultrathin GSs are fabricated by sonication of expanded graphite in N-methyl-2-pyrrolidone (NMP). Expanded graphite is produced as a raw material for packings and seals by rapid heating of expandable graphite at 800 °C~ 1000 °C for 300 ~ 10 s in air. Byproducts after stamping these products out of thick GSs can also be used after pulverization instead of raw expanded graphite. Expandable graphite is natural flake graphite after intercalation of sulfuric acid. NMP was reported to exfoliate graphite by sonication,[27] and use of expanded graphite with partly exfoliated structures is considered to increase the yield of ultrathin GSs. Composites of the two dimensional Si nanopowder and GSs are found to improve the cyclability and mass loadings of Si electrodes, and the reaction mechanisms are investigated during 300 cycles.

Experimental

Materials.—Si swarf generated during slicing of solar cell grade n-type Si ingots (1~2 Ω·cm) by use of the fixed abrasive machining technology with water-based coolant was used as the starting material. Si swarf was partly deagglomerated by a crusher. Si/GS composites were fabricated by sonicating Si nanopowder and GSs at the weight ratio of 5:1 in NMP for 2 h and filtering the solution. GS dispersion was prepared by sonicating expanded graphite (EC10, Ito Graphite Co., Ltd.) in NMP for 20 h. C-coated Si nanopowder (C/Si = 0.1wt) was fabricated by annealing Si nanopowder at 1000 °C under H_2 atmosphere, followed by annealing it under C_2H_4 (99.5%) atmosphere.[6,7]

Cell constructions.—Si/GS composites, C-coated Si nanopowder or pristine Si nanopowder with the theoretical capacities of 3044 mAh g^{-1}, 3287 mAh g^{-1} or 3578 mAh g^{-1}, respectively, was mixed with Ketjen black (KB, EC-300J, Lion Co. Ltd.), binder polymers of 4 wt% cross-linked poly(acrylic acid) (CLPA) and 2 wt% poly(vinyl alcohol) (PVA) dissolved in pure water with the weight ratio of 60:20:10:10. Copper foil was coated with the slurry, and dried in the air. After cutting the electrode sheets into circles (11.3 mm in diameter), the electrodes were dried at 150 °C under vacuum for 6 h.

[z]E-mail: tmatsumo@sanken.osaka-u.ac.jp

The mass loading of Si/GS composites and C-coated Si nanopowder was set at ~0.65 mg cm^{-2} for experiments to investigate the reaction mechanisms. The thickness of the electrode was ~15 μm as observed by the scanning electron microscopy (SEM). CR2032-type coin cells were assembled with a Si electrode, a lithium foil (battery grade) as a counter electrode, a polyethylene separator, and an electrolyte of 1 M $LiPF_6$ in a mixture of ethylene carbonate (EC) and diethyl carbonate (DEC) (1:1 by volume) (battery grade, Kishida Chemicals Co. Ltd.) with 10 wt% fluoroethylene carbonate (FEC).

Cell characterization.—The cells were cycled in the cell voltage range between 0.01 and 1.5 V during 300 cycles using a battery charge/discharge unit (SD8, Hokuto Denko Co.). 1C rates were set at 3044 mA g^{-1} (2.0 mA cm^{-2}), 3287 mA g^{-1} (2.1 mA cm^{-2}) and 3578 mA g^{-1} (2.3 mA cm^{-2}) for the Si/GS, C-coated Si and pristine Si electrodes, respectively. The lithiation and delithiation current densities were set at 0.05 C for the first 5 cycles to amorphize Si, and 0.5 C for the afterward 295 cycles. Electrochemical impedance spectroscopy (EIS) measurements were performed using a potentiostat/galvanostat/frequency response analyzer (VSP, BioLogic) with 5 mV amplitude perturbation and the frequency range between 1 M and 1 Hz after the lithiation at 0.01 V. The impedance data were analyzed using an EC-Lab software program. TEM, scanning TEM (STEM) and energy dispersive X-ray spectroscopy (EDS) mapping images were obtained using a JEOL JEM-ARM 200 F microscope with the 200 keV incident electron energy. SEM images were observed using a JEOL JSM-6335F field emission scanning electron microscope. Cross sections of the Si electrodes were observed after ion milling with Hitachi IM4000. Electrodes after lithiation/delithiation cycles were observed after washing them with DEC and ethanol. X-ray diffraction (XRD) measurements were used to check the average crystallite sizes with Rigaku SmartLab. Raman spectra were acquired with a JASCO NR-1800. The excitation light wavelength, power and exposure time were 532 nm, 20 mW and 15 min, respectively. The resolution of the spectrometer and accumulation number were 3 cm^{-1} and 2, respectively. The spectra were smoothed by the Savitzky-Golay method over the convolution width of 17 points. Thermogravimetry was performed with a Rigaku TG-8120 at the heating rate of 5 °C min^{-1}.

Results

Structure of active materials.—Figure 1a shows the SEM image of Si nanopowder after crushing. Agglomerates of large flake-shaped Si nanopowder of 9 ~ 40 nm thickness and 60 nm~2 μm lateral size were observed. A TEM image also showed flake-shaped Si nanopowder of a few tens nanometers ~ 1.1 μm lateral size (Fig. 1b). The diffraction pattern with sharp spots indicates that the area indicated by the circle is assigned to a single crystalline Si. Small Si flake-shaped nanopowder of a few to a few tens nanometer lateral size stacked on large Si nanopowder (Fig. 1c). The thickness of the Si nanopowder was 2 ~ 10 nm as observed in the TEM image from the thickness direction (Fig. 1d). The average crystallite sizes of Si nanopowder were estimated to be 34, 27 and 24 nm from the (111), (220) and (311) XRD peaks, respectively, in Fig. S1a (available online at stacks.iop.org/JES/168/020521/mmedia) with the Scherrer's equation. The anisotropic crystallite sizes correspond to the nanoflake shapes of Si crystallites. The mode and median diameters of Si nanopowder were estimated to be 29.0 and 36.1 nm, respectively, from the shape of the Si(111) peak using the lognormal size distribution (SLN profile) method[28] (Fig. S1b). A small C(200) peak at 26.6° for Si nanopowder is assigned to swarf from graphite plates that support Si ingots. The weight ratio of graphite swarf is less than a few percent. The graphite swarf can be removed easily in water but the electrode performances show negligible differences (Fig. S1a). Figure S2a shows a Raman spectrum for Si nanopowder. A peak measured at 519 cm^{-1} is assigned to crystalline Si.[29,30] No peak assignable to a-Si was observed at ~480 cm^{-1}.[30] These results indicate Si nanopowder does not contain a-Si.

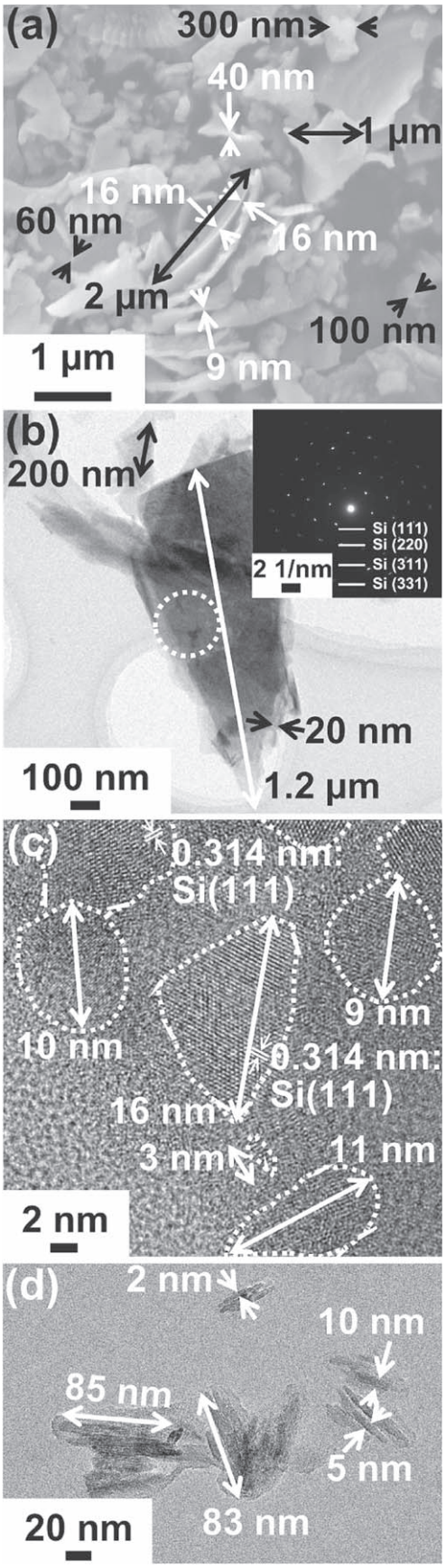

Figure 1. SEM image of Si nanopowder (a), and TEM images of large Si nanopowder (b), small Si nanopowder around an edge of large Si nanopowder (c), and Si nanopowder observed from the thickness direction (d). The inserted electron diffraction pattern was observed at the area indicated by the circle.

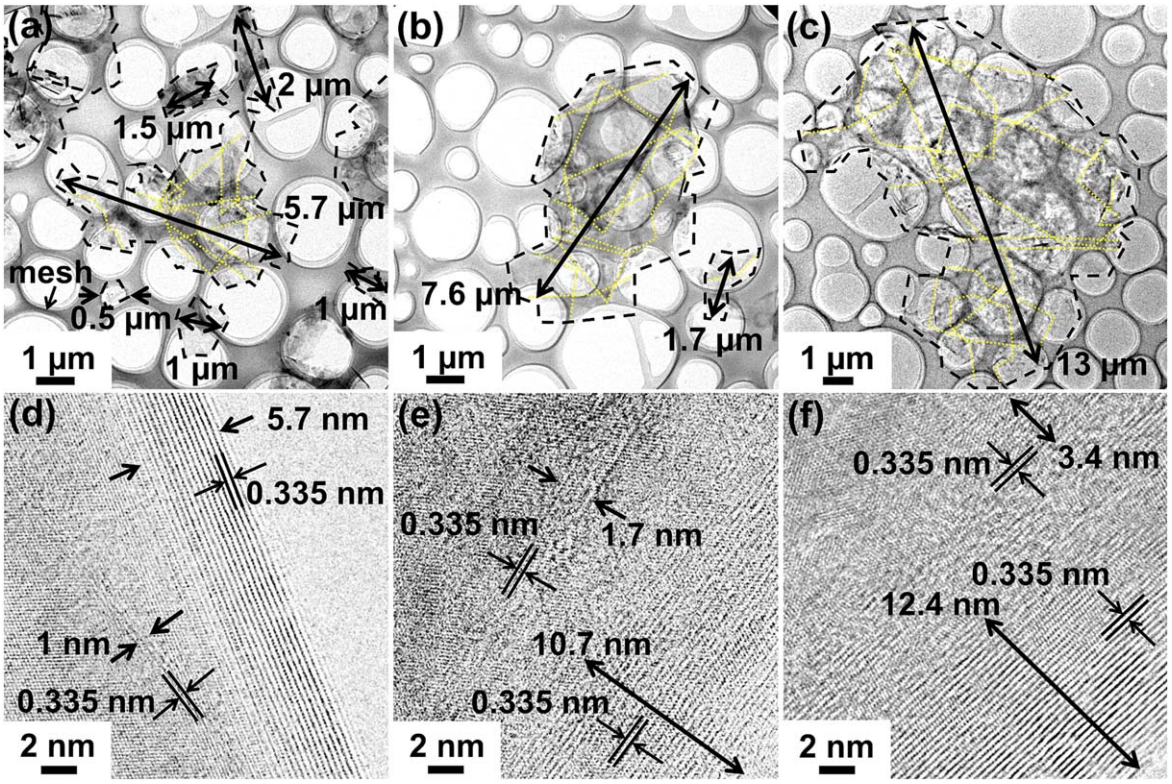

Figure 2. TEM images of graphite sheets in the top (a), middle (b) and bottom (c) parts of the NMP dispersion. High resolution TEM images of the rolled edges for graphite sheets in figures (a)∼(c) are shown in figures (d)∼(f), respectively. The yellow dotted lines indicate edges of overwrapped graphite sheets.

Table I. Size, thickness and weight ratio of graphite sheets dispersed in NMP.

	Average size (μm) (maximum∼minimum)	Average thickness (nm) (maximum∼minimum)	Weight ratio
Top	2.6 (5.7 ∼ 0.5)	4.7 (9.1 ∼ 1.0)	1
Middle	7.6 (9.0 ∼ 1.7)	6.1 (13.4 ∼ 1.7)	10
Bottom	10.4 (13.0 ∼ 9.0)	7.6 (13.0 ∼ 2.0)	10

Figure 2 shows typical TEM images of GSs fabricated from expanded graphite by sonication in NMP. Roughly 3 stage gradation of darkness was observed for the GS dispersion 30 min after sonication. The GSs in Figs. 2a–2c were obtained from the top, middle and bottom parts of the GS dispersion, respectively. The average diameter of the GSs increased from 2.6 μm to 10.4 μm depending on the sampling depth (Table 1). Many dark lines observed in Figs. 2a–2c were assigned to rolled edges of GSs as shown in Figs. 2d–2f, respectively. GS edges showed atomic layers of GSs with the separation of 0.335 nm. The average thickness of the GSs increased from 4.7 nm to 7.6 nm depending on the sampling depth. An XRD pattern for GSs showed two clear peaks that are assigned to (002) and (004) of graphite. The mode and median diameters of dried GSs were calculated to be 28.2 and 38.0 nm, respectively, from the shape of the C(002) peak using the SLN profile method [28] (Fig. S1b). The Raman spectrum of GSs showed a peak at 1580 cm^{-1} assigned to the G-band of graphite, while the D-band or D'-band peaks induced by defects at ∼1350 or 1620 cm^{-1}, respectively, were absent (Fig. S2b).[31,32] It was indicated that GSs were hardly damaged during the fabrication processes.

Figure S3 shows the TEM (a) and EDS mapping (b and c) images of the Si/GS composites. Si nanopowder was dispersed between GSs without agglomeration. Figure S4 shows the TEM (a and c) and EDS mapping (b) images of C-coated Si nanopowder. An amorphous (a-)C layer of ∼10 nm thickness was observed on agglomerated Si

Table II. Delithiation capacities and the retention rates of the Si/GS composite, C-coated Si and pristine Si electrodes.

	Delithiation capacity					
	Si/GS		C coated-Si		pristine Si	
	(mAh cm^{-2})	(mAh g^{-1})	(mAh cm^{-2})	(mAh g^{-1})	(mAh cm^{-2})	(mAh g^{-1})
6th cycle	1.69	2596	1.55	2385	0.09	135
100th cycle	1.20	1841	1.17	1802	0.03	53
300th cycle	0.83	1273	0.72	1114	0.03	50
Retention rate (6 ∼ 300th)	49.1%		46.5%		33.3%	

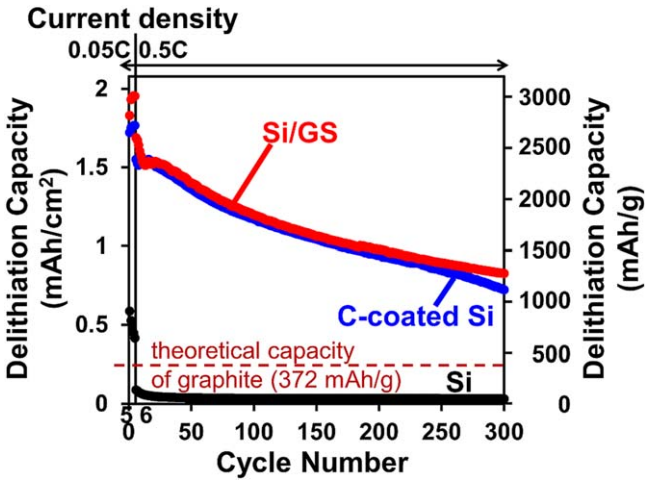

Figure 3. Delithiation capacity vs cycle number for the Si/GS, C-coated and pristine Si electrodes.

nanopowder of a few micrometer size. The Raman spectrum for C-coated Si showed a large and broad peak at 1343 cm^{-1} assigned to the D-band, indicating that formed C layer is mainly amorphous (Fig. S2b). Small peaks at 1583 and 1615 cm^{-1} are assigned to the G-band and D'-band that correspond to layered structures observed in domains smaller than a few nanometers.

Figure S5 shows TG curves for Si nanopowder, C-coated Si, Si/GS composites and GSs. GSs and an a-C layer were removed from 600 °C to 830 °C by oxidation in air, and Si was completely oxidized from 750 °C to 1450 °C. The composition of Si nanopowder, Si/GS composites, C-coated Si, and their roughly estimated theoretical capacities were summarized in Table SI. The weight ratio of Si/SiO_2 in Si nanopowder was estimated to be 96/4. The weight ratios of C in the Si/GS composites and C-coated Si nanopowder were corrected with the increase in the weight of Si nanopowder by oxidation up to ∼800 °C. The measured weight ratios of C and Si were close to those of input materials. SiO_2 is assigned to native oxide on Si nanopowder.

Cell performance.—Figure 3 shows the delithiation capacities of the Si/GS, C-coated Si and pristine Si electrodes with the theoretical capacities of 1.98 mA cm^{-2}, 2.14 mA cm^{-2} and 2.33 mA cm^{-2}, respectively. For the Si/GS electrode, the delithiation capacity at the 5th cycle was 1.95 mAh cm^{-2} close to the theoretical capacity. The delithiation capacity dropped sharply to 1.69 mAh cm^{-2} at the 6th cycle and to 1.52 mAh cm^{-2} at the 12th cycle. The Si/GS electrode showed mostly higher delithiation capacity compared with that of the C-coated Si electrode. The degradation of the C-coated electrode was accelerated after ∼180 cycles. The pristine Si electrode was uncompetitive due to the low capacity of ∼0.07 mAh cm^{-2} at the 10th cycle. The delithiation capacity at the 300th cycle and the retention rate for the 6th∼300th cycles for the Si/GS electrode were 0.83 mAh cm^{-2} and 49.1%, respectively, which were the highest among the three electrodes (Table II). GSs were found to improve the cyclability of a Si electrode compared with an a-C layer on Si nanopowder. The C-coated Si electrode with the C/Si ratio of 0.2 was fragile and showed lower delithiation capacities probably due to agglomeration of Si nanopowder during C coating and peeling-off of Si during cycles as reported previously.[7]

Figures 4a and 4c show the lithiation and delithiation curves, respectively, for the Si/GS electrode at the 6th cycle. Both curves were divided into the regions of (ii)∼(iv) and (vii)∼(ix) in which difference between the cell voltage and the tangent line was less than 0.003 V. Figures 4b and 4d show the dQ/dV curves, and the peak minima and maxima correspond to the tangential contact points. The regions of (i)∼(x) are often categorized into 5 regions as reported previously.[6,33–37] Region A and B were reported to relate with formation of a-$Li_{2.5}Si$ from Si and formation of a-Li_xSi ($2.5 < x < 3.75$) with an outermost crystalline (c-)$Li_{15}Si_4$ layer, respectively. Region C, D and E were assigned to delithiation of a-Li_xSi ($2.5 < x < 3.75$) to a-Li_2Si, delithiation of c-$Li_{15}Si_4$ and a-Li_2Si to a-Li_xSi ($0 < x \leqslant 2$), and formation of a-Si, respectively.

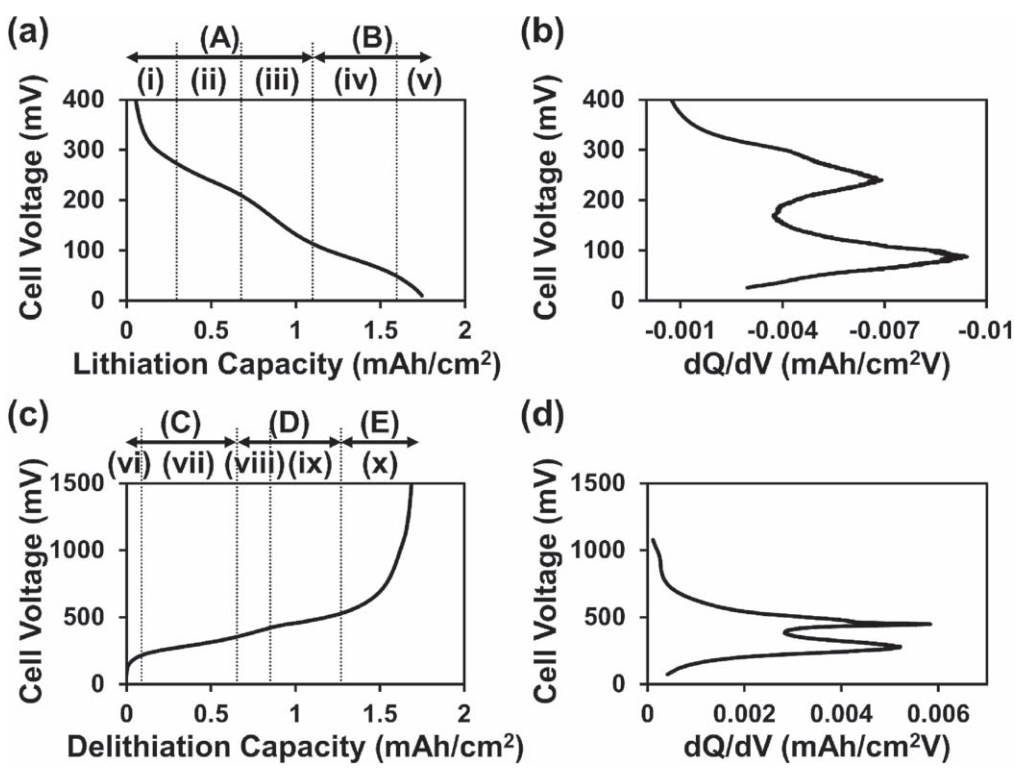

Figure 4. Lithiation (a) and delithiation (c) curves for the Si/GS composite electrode at the 6th cycle. The dQ/dV curves for the curves in figures (a) and (c) are shown in figures (b) and (d), respectively.

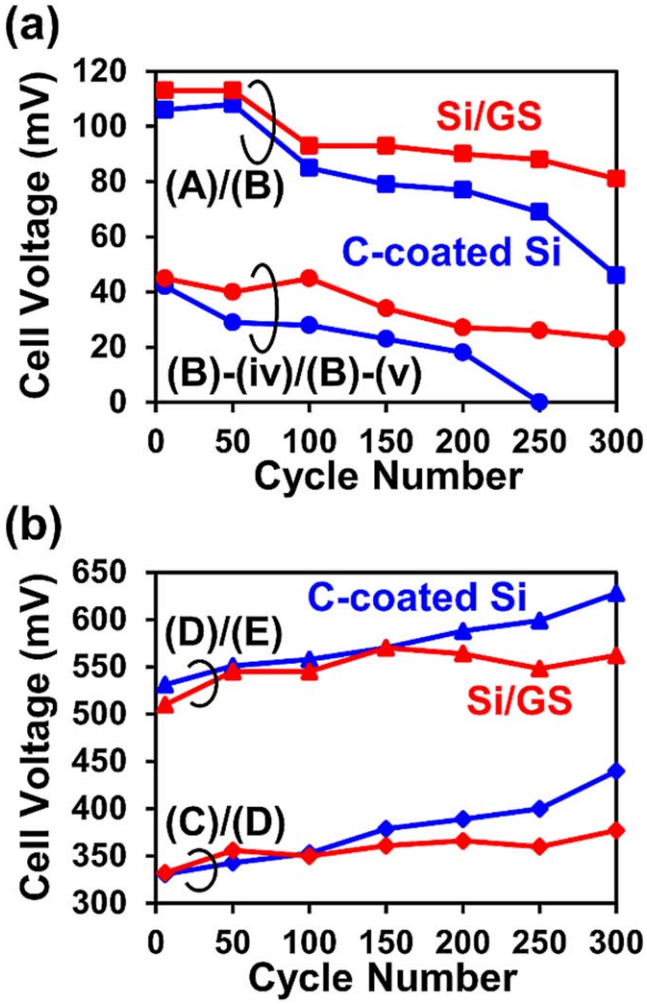

Figure 5. Cell voltages at the end of region A and B-iv (figure (a)) and region C and D (figure (b)) for the Si/GS and C-coated Si electrodes.

Figure 5 shows the cell voltages at the region boundaries for the Si/GS and C-coated Si electrodes. The cell voltage decreases and increases during lithiation and delithiation of Si, respectively, due to the overvoltage. Lower overvoltages are measured for the Si/GS electrode during lithiation, and from the 150th cycle during delithiation.

Figure 6 shows the lithiation and delithiation capacities in region A ∼ E for the Si/GS and C-coated Si electrodes vs the cycle number. The capacities at the 6th and 300th cycles, the decreases in the capacity during the 6th∼300th cycles and the retention rates in region A ∼ E are summarized in Table III. In region A, the lithiation capacity decreased similarly from ∼1.1 mAh cm^{-2} at the 6th cycle to 0.49 ∼ 0.56 mAh cm^{-2} at the 300th cycle for both Si electrodes. In region B, the lithiation capacity of the Si/GS electrode was higher than that of the C-coated Si electrode except for the 50th cycle. Lithiation in region B-v was not observed from the 250th cycle for the C-coated Si electrode. In region C, the Si/GS electrode showed the higher delithiation capacity. In region D, the delithiation capacity of the C-coated Si electrode was higher presumably due to the higher theoretical capacity of the C-coated Si electrode. In region E, the retention rates of the delithiation capacity during the 6th∼300th cycles were only ∼20% for both Si electrodes, which is significantly lower than those in region A ∼ D.

Electrochemical impedance analysis.—Figure 7 shows the Nyquist plots for the Si/GS and C-coated Si electrodes after the 6th and 300th cycles. These plots were well fitted using the equivalent circuit to evaluate the internal resistances. The series resistance (R_s), the solid electrolyte interphase (SEI) resistance (R_{SEI}) and the charge transfer resistance (R_{ct}) are summarized in Table IV. R_s for the Si/GS electrode were only a half and two-thirds of R_s for the C-coated Si electrode at the 6th and 300th cycles, respectively. R_{ct} for the Si/GS electrode was also two-thirds of R_{ct} for the C-coated Si electrode at the 300th cycle. Similar R_{ct} at the 6th cycle and R_{SEI} were measured for both Si electrodes. These results suggest that R_s was greatly improved and the increases in R_s and R_{ct} at the 300th cycle were suppressed by GSs.

Structure of Si electrodes.—Figure 8 shows the cross-section TEM and EDS mapping images of the Si/GS electrode before cycles. Typical Si flakes between GSs and an area indicating a cross-section of a layered structure of ∼170 nm thickness were observed in Fig. 8a. A magnified image showed bright straight lattice fringes in the angular areas highlighted by the yellow dotted lines (Fig. 8b). In the surrounding areas, lattice fringes are bent as indicated by the arrows. From the lattice fringe spacing, the areas highlighted by the yellow dotted lines are assigned to a single crystalline Si nanoflake of 0.314 nm lattice fringe spacing corresponding to (111) planes of Si, while the surrounding areas are assigned to GSs of 0.335 nm spacing corresponding to (002) planes of graphite (Figs. 8c and 8d). Ultrathin GSs of a few nanometer thickness closely capsulated Si nanoflakes of a few nanometer thickness, which is feasible to improve contacts between Si nanopowder and ultrathin GSs and supply many conductive paths.

Figure 9 shows the surface SEM images of the Si/GS and C-coated Si electrodes before cycles and after the 100th and 300th cycles. For the Si/GS electrode, integration of Si flakes and GSs were observed before cycles (Fig. 9a). GS bridges of 3 ∼ 10 nm thickness were formed across a shallow crack. After the 100th cycle, GS bridges contacting with Si nanoflakes were formed across deep cracks as indicated by EDS mapping images (Fig. 9b). After the 300th cycle, the number of the cracks increased but the GS bridges suppressed crack formation as indicated by arrows (Figs. 9c and 9d). For the C-coated Si electrode, agglomerates of C-coated Si and KB (Fig. 9e) cracked after the 100th cycle (Fig. 9f). The width of the cracks increased after the 300th cycles (Fig. 9g), and bridging structures were not observed in the C-coated Si electrode (Fig. 9h).

Figure 10 shows the cross-section SEM images of the Si/GS and C-coated Si electrodes. In the Si/GS electrode, thick GSs of 25 ∼ 80 nm thickness wrapped the Si/GS composites, and KB partly filled spaces before cycles (Fig. 10a). In the magnified SEM image, cross sections of the Si/GS composites with a layered structure along a thick GS as highlighted by a yellow dotted line, and the surfaces of the layered structure were observed. After the 100th cycle, thick GSs wrapped the partly fused Si/GS composites (Fig. 10b), and the magnified image showed the layered structure (Fig. 10c). The electrode was contacted closely with the Cu collector. After the 300th cycle, thick GSs closely contacted with Si/GS composites (Fig. 10d). The layered structure indicated by the arrows and the spaces of width less than 100 nm were observed without obvious changes. In the C-coated Si electrode, the agglomerated structure of C-coated Si and KB (Fig. 10e) changed to the wrinkle structure after the 100th cycle (Fig. 10f). The wrinkle structure was reported to mainly consist of Si frameworks (Fig. 10g), resulting in higher capacities.[6,38] After the 300th cycle, most of the pores disappeared, indicating fusion of Si (Fig. 10h).

Figure 11 shows STEM and EDS mapping images of the Si/GS and C-coated Si electrodes. For the Si/GS electrode, dispersed Si nanopowder and KB were wrapped by ultrathin GSs before cycles (Fig. 11a) as observed in Fig. 10a. After the 100th cycle, Si nanopowder was dispersed between the GSs, and the wrinkle structure were partly observed in large Si nanopowder (Fig. 11b). Though the wrinkle structure disappeared after the 300th cycle, Si nanopowder was still dispersed between the GSs (Fig. 11c). For the C-coated Si electrode, agglomerates of C-coated Si before cycles

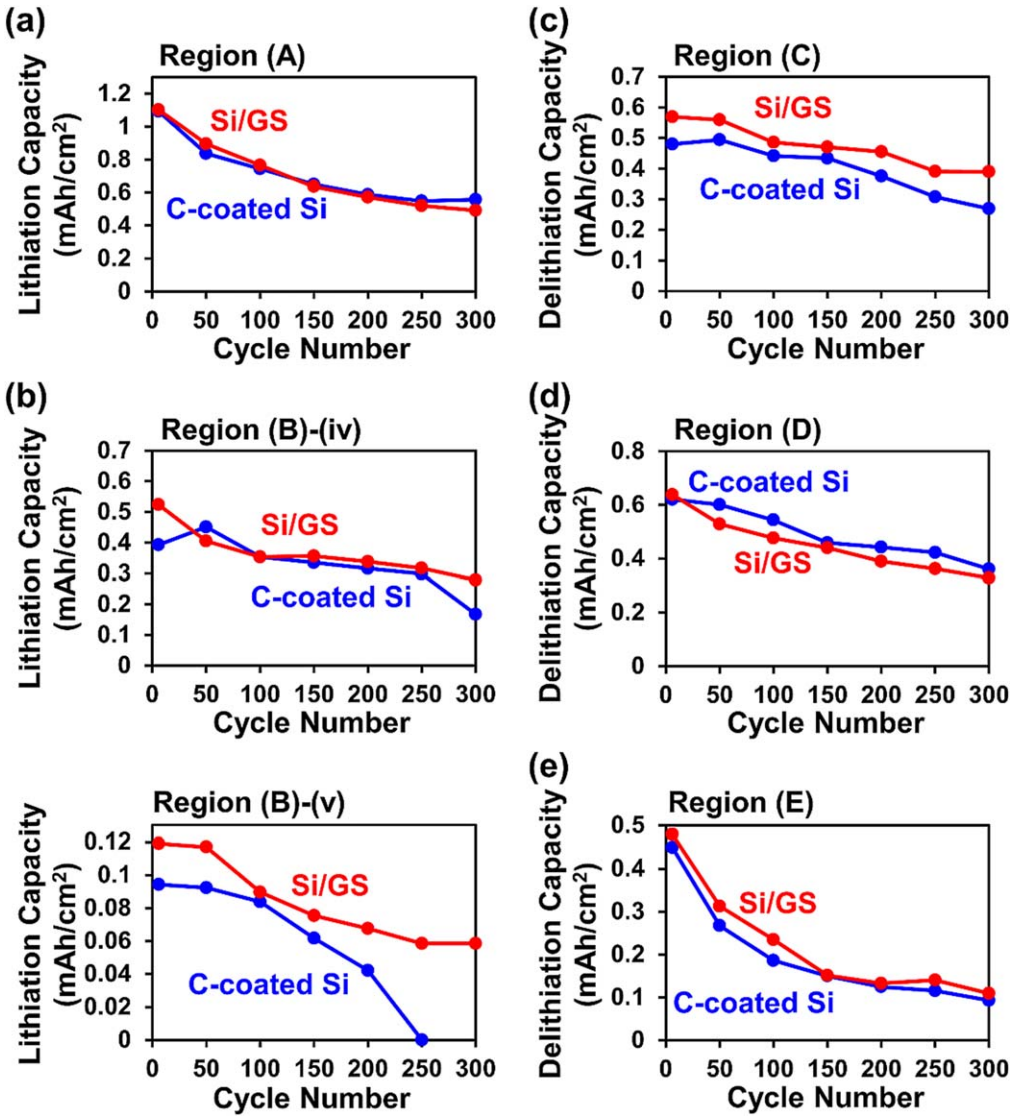

Figure 6. Lithiation and delithiation capacities in region A ∼ E vs the cycle number for the Si/GS and C-coated Si electrodes.

(Fig. 11d) showed the wrinkle structure after the 100th cycle (Fig. 11e), and a fused Si structure was mainly observed after the 300th cycle (Fig. 11f). After the 300th cycle, Si was completely amorphized in the Si/GS composite and C-coated Si electrodes as indicated by dim rings without spots in the SAED patterns.

Limitation of delithiation capacity.—Figure 12 shows the delithiation capacities of the Si/GS and C-coated Si electrodes with the delithiation limitation at 1200 mAh g^{-1} after deep lithiation at 0.01 V. The delithiation limitation was found to avoid large shrinkage of the Si electrodes.[6] The areal delithiation capacity for the Si/GS electrode kept 0.8 mAh cm^{-2} until the 901st cycle, while that for the C-coated Si electrode kept 0.8 mAh cm^{-2} until the 660th cycle.

Thick electrodes.—Figure 13 shows the delithiation capacities of the Si/GS and C-coated Si electrodes with higher loading masses. The mass loading of the active materials was increased from 0.65 mg cm^{-2} to 1.97 mg cm^{-2} for the Si/GS electrode and to 1.82 mAh cm^{-2} for the C-coated Si electrode. The current density at the 1st cycle was set at 0.05 C. From the 2nd cycle, the Si/GS and C-coated Si electrodes were lithiated at the constant voltage of 0.01 V for 60 and 75 min, respectively, between lithiation and delithiation at 0.5 C. The areal delithiation capacity at the 50th cycle increased from 1.4 mAh cm^{-2} to 1.9 mAh cm^{-2} for the Si/GS electrode, while decreased to 1 mAh cm^{-2} for the C-coated Si electrode.

With the limited delithiation at 1200 mAh g^{-1}, the time for lithiation at the constant voltage of 0.01 V were set at 90 and 60 min for the Si/GS and C-coated Si electrodes, respectively. For the Si/GS electrodes, the mass loadings of the active materials were increased to 1.97 and 3.29 mg cm^{-2}, corresponding to the areal capacities of 6 and 10 mAh cm^{-2}, respectively. The delithiation capacities at 2.4 and 4 mAh cm^{-2} after lithiation at 0.01 V kept 1200 mAh g^{-1} for more than 100 and 75 cycles, respectively. The current densities also increased to 2 and 5 mA cm^{-2}. For the C-coated Si electrode with the mass loading of 1.73 mg cm^{-2}, the delithiation capacity kept 1200 mAh g^{-1} (2.1 mAh cm^{-2}) until the 16th cycle.

Discussion

GSs suppressed the overvoltage of the Si electrode by 3 ∼ 35 mV compared with an a-C layer (Fig. 5). The lithiation capacity can increase by 0.02 ∼ 0.04 mAh cm^{-2} with a decrease in the overvoltage by 5 mV because region B is mainly composed of the

Table III. Lithiation and delithiation capacities at the 6th and 300th cycles, the decreases in the capacities during the 6th∼300th cycles, and the retention rates in region A ∼ E.

Region	Electrode	Capacity at the 6th cycle (mAh cm^{-2})	Capacity at the 300th cycle (mAh cm^{-2})	Decrease in capacity (mAh cm^{-2})	Retention rate (6th∼300th)
A	Si/GS	1.10	0.49	0.61	45
	C-coated Si	1.09	0.56	0.54	51
B	Si/GS	0.64	0.34	0.31	52
	C-coated Si	0.49	0.17	0.32	34
C	Si/GS	0.57	0.39	0.18	69
	C-coated Si	0.48	0.27	0.21	56
D	Si/GS	0.64	0.33	0.31	51
	C-coated Si	0.62	0.36	0.26	58
E	Si/GS	0.48	0.11	0.37	23
	C-coated Si	0.45	0.09	0.36	21

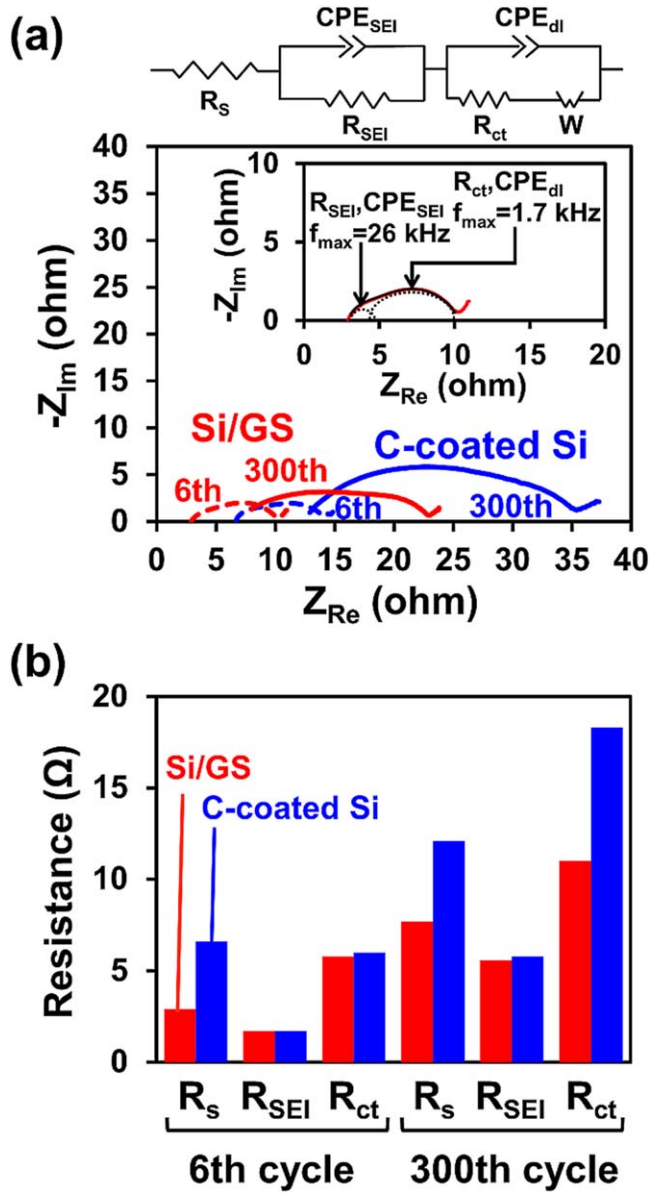

Figure 7. Nyquist plots for the Si/GS and C-coated Si electrodes after the 6th and 300th cycles and the equivalent circuit used for fitting plots (a), and internal resistances (b).

Table IV. Internal resistances for the Si/GS composite and C-coated Si electrodes after the 6th and 300th cycles.

Electrode	Cycle	R_s (Ω)	R_{SEI} (Ω)	R_{ct} (Ω)	Total (Ω)
Si/GS composite	6th	2.9	1.7	5.8	10.4
	300th	7.7	5.6	11	24.3
C-coated Si	6th	6.6	1.7	6.0	14.3
	300th	12.1	5.8	18.3	36.2

plateau region (Fig. 4a). For the Si/GS electrode, the low overvoltage increased the lithiation capacity, resulting in the higher delithiation capacity in region C (Fig. 6b and Table III).

The overvoltage for the Si/GS electrode mostly lower than that for the C-coated Si electrode, which is partially attributed to low R_s (Table IV). The increase in the overvoltage was suppressed from the 150th cycle for the Si/GS electrode because of the less increases in

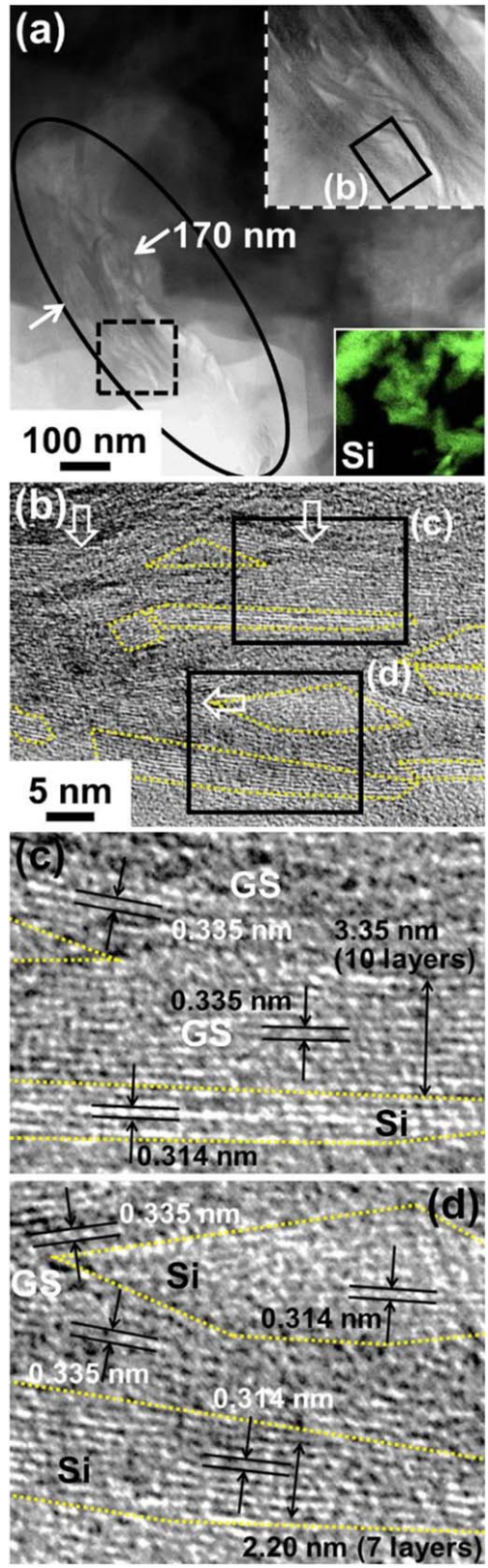

Figure 8. Cross-section TEM and EDS mapping images of the Si/GS electrode before cycles. (a) Cross-section of a Si/GS composite. A layered structure was observed in the area indicated by the ellipse. The insets are the magnified TEM image of the area indicated by the dotted square, and the EDS mapping image. (b) High resolution TEM image of the areas indicated in figure (a). Lattice fringes are bent around the places indicated by arrows. (c) and (d) Magnified images of the area indicated by the rectangles.

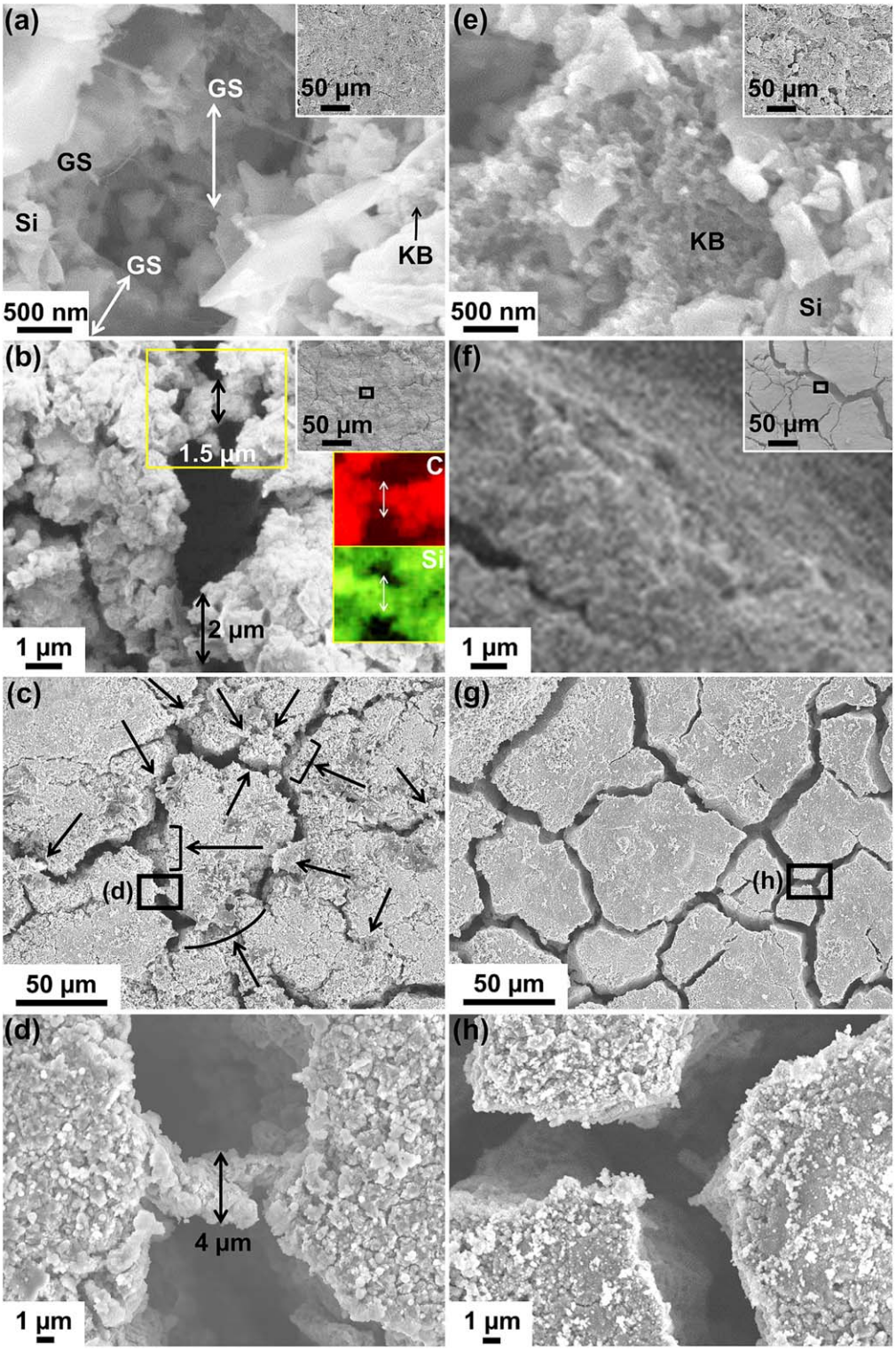

Figure 9. Surface SEM images of the Si/GS electrode before cycles (a), after the 100th cycle (b) and after the 300th cycle (c and d), and the C-coated Si electrode before cycles (e), after the 100th cycle (f) and after the 300th cycle (g and h). The SEM images in figures (b) and (f) were observed in the area indicated by the rectangles in the insets. An EDS mapping image of a bridge structure is shown in figure (b). The SEM images in figures (d) and (h) were observed at the area indicated by the rectangles in figures (c) and (g), respectively. The arrows in figures (a)∼(d) indicate bridge structures.

R_s and R_{ct}. The mechanisms of these behaviors can be explained by differences in the electrode structures as follows.

Figure 14 shows a schematic draw of the structural changes in the Si/GS and C-coated Si electrodes depending on the cycle number. The Si/GS electrode is composed of the layered Si/GS composites wrapped by the thick GSs (Figs. 10a, 10b and 10d). Si flakes are well dispersed between ultrathin GSs (Figs. 8 and 11a), resulting in high electrical conductivity (Fig. 6 and Table III). During 100 cycles, the Si/GS composites partly fuse and the wrinkle structure is partly formed (Figs. 10b, 10c and 11b). After the 300th cycle, the wrinkle

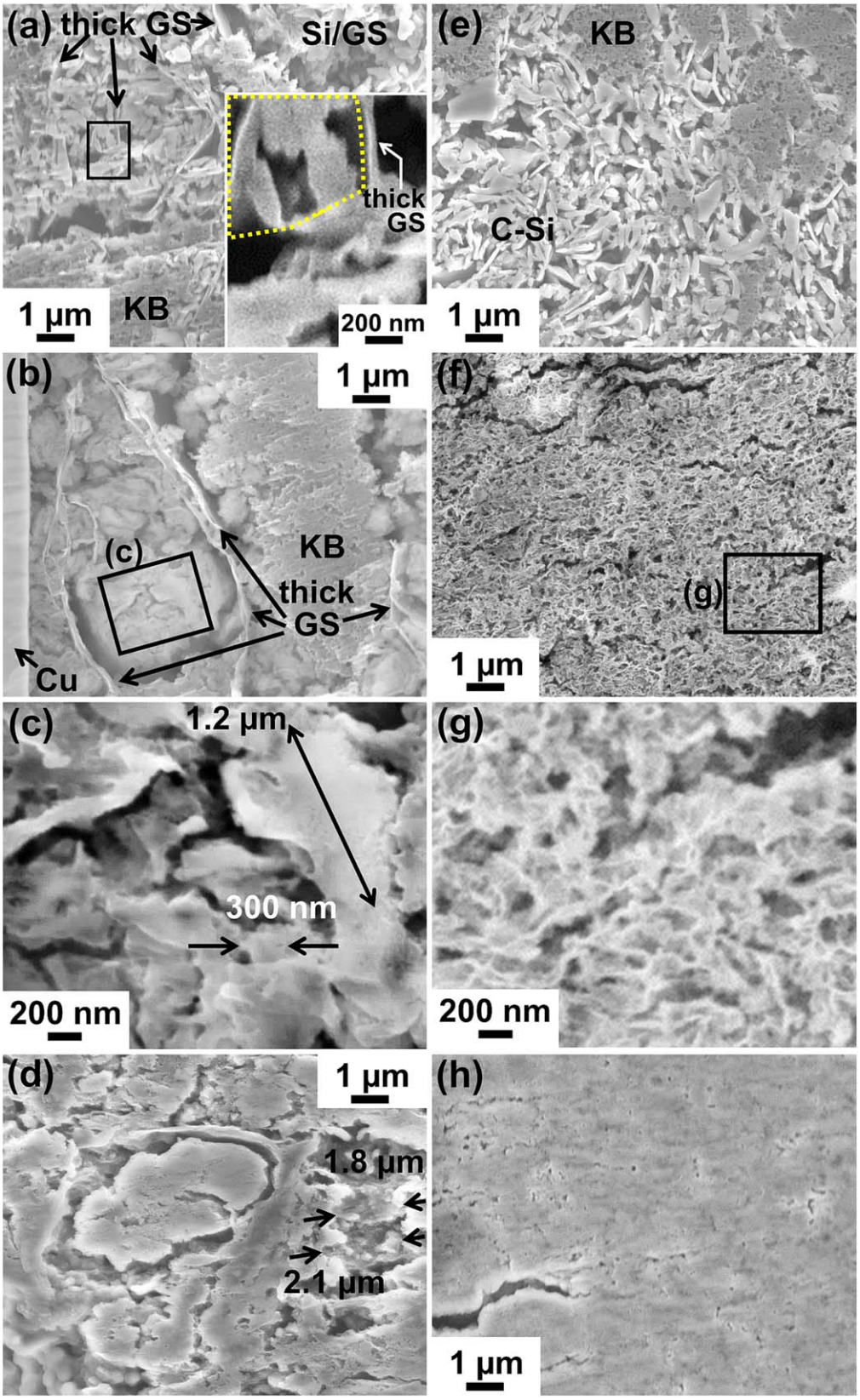

Figure 10. Cross-section SEM images of the Si/GS electrode before cycles (a), after the 100th cycle (b and c) and after the 300th cycle (d), and the C-coated Si electrode before cycles (e), after the 100th cycle (f and g) and after the 300th cycle (h). The inserted high resolution SEM images were observed in the area indicated by the rectangles in figure (a). The area highlighted by the yellow dotted line showed Si/GS composites aligned along a thick graphite sheet. Figures (c) and (g) are high-resolution SEM images of the indicated area in figures (b) and (f), respectively.

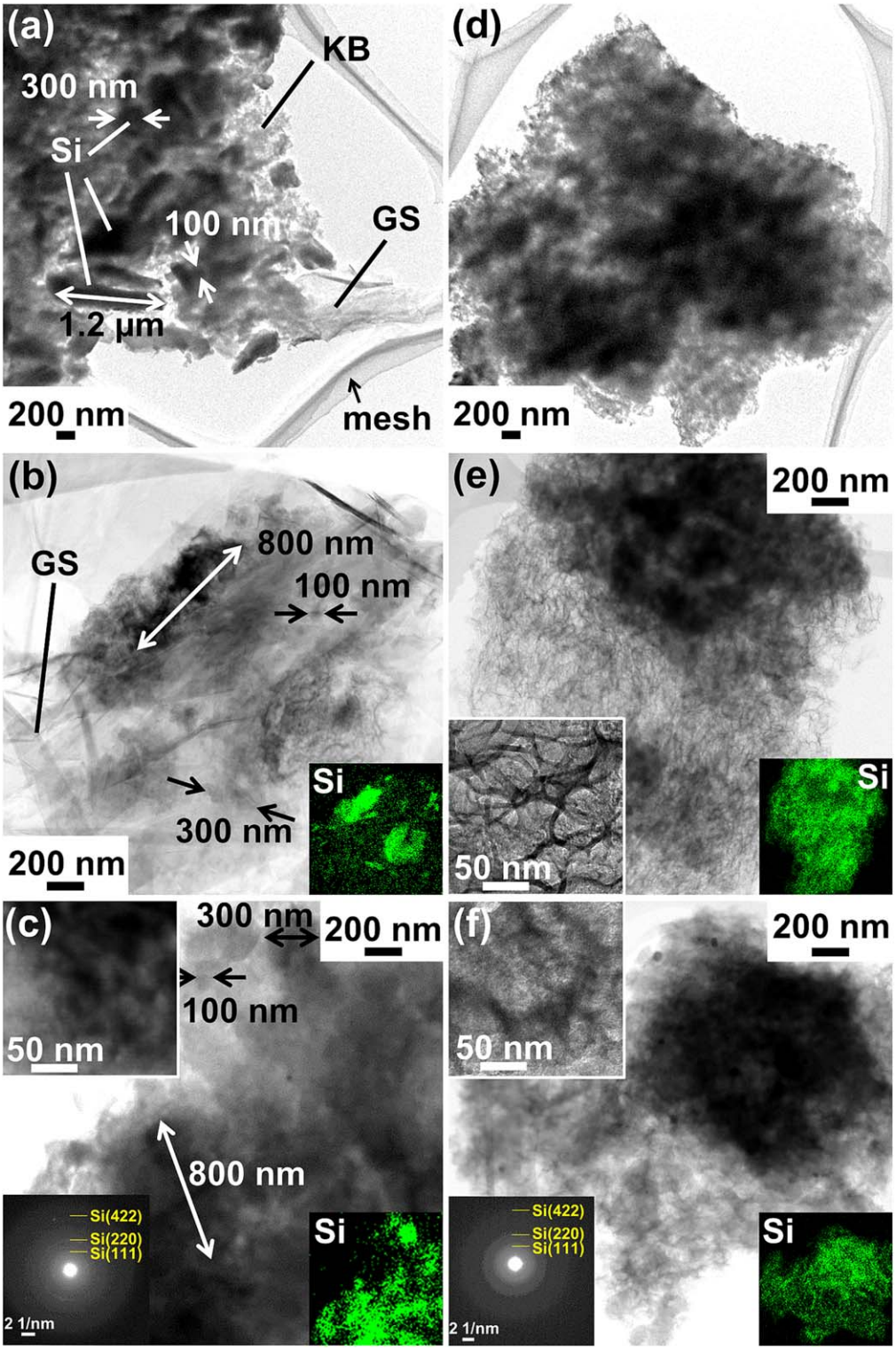

Figure 11. STEM and EDS mapping images of the Si/GS electrode before cycles (a), after the 100th cycle (b) and after the 300th cycle (c), and the C-coated Si electrode before cycles (d), after the 100th cycle (e) and after the 300th cycle (f). High-resolution TEM images are shown in figures (c), (e) and (f). SAED patterns are also shown in figures (c) and (f).

structure is absent without significant fusion of Si nanopowder (Fig. 11c). The ultrathin GSs bridge across the cracks with suppressing crack formation and peeling-off of Si (Figs. 9c and 9d), while the thick GSs work as stable conductive frameworks that also secure electrolyte paths and buffer spaces for large Si volume changes (Figs. 10a∼10d). Low R_s and suppression of increases in R_s and R_{ct} during cycles are achieved by these functions of GSs. In the case of the C-coated Si electrode, the homogeneous wrinkle structure with a large surface area are formed before the 100th cycle (Figs. 10f, 10g and 11e). After the 300th cycle, fusion of Si restricts electrolyte paths and electrode

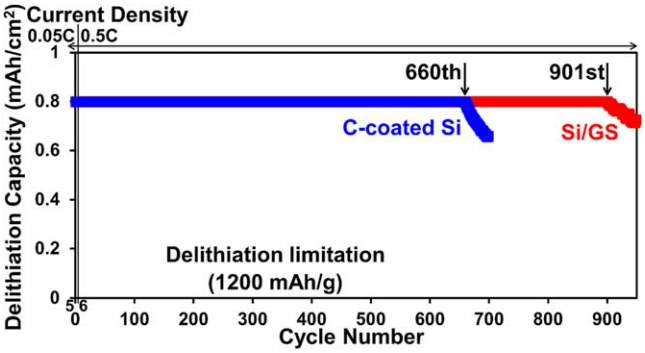

Figure 12. Delithiation capacity vs cycle number for the Si/GS and C-coated Si electrodes with the delithiation limitation at 1200 mAh g^{-1} after lithiation to 0.01 V.

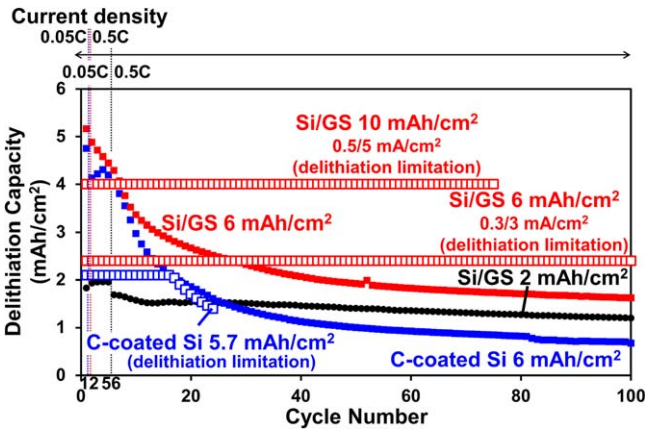

Figure 13. Delithiation capacity vs cycle number for thick Si/GS and C-coated Si electrodes with and without delithiation limitation at 1200 mAh g^{-1}. Lithiation periods at the constant voltage of 0.01 V were 60 min for the thick Si/GS electrode without delithiation limitation and the C-coated Si electrode with delithiation limitation, 75 min for the C-coated Si electrode without delithiation limitation, and 90 min for the Si/GS electrodes with delithiation limitation.

surface area (Figs. 10h and 11f), resulting in the increases in R_s and R_{ct}, respectively (Fig. 7 and Table IV).[39]

For the Si/GS electrode, the delithiation capacity decreased from 1.95 mAh cm^{-2} to 1.69 mAh cm^{-2} at the 6th cycle due to the increase in the current density. This is because the overvoltage increases linearly with the current density at a constant resistance. The subsequent decrease in the delithiation capacity until the 12th cycle is probably due to stress during inhomogeneous lithiation and delithiation of Si[7,40] and consequent peeling-off and electrical isolation of Si nanopowder.

The capacity retention rates for the Si/GS electrode and the C-coated electrode in region E during the 6th∼300th cycles were only 23% and 21%, respectively, which is almost less than a half of 45 ∼ 69% in region A ∼ D except for region B of the C-coated Si electrode. The low retention rates of the delithiation capacities can be attributed to electrical isolation of Si nanopowder caused by degradation of the inter-particle contacts with large shrinkage of Si in region E.[6,41] The inter-particle contacts partly recovered with expansion of Si nanopowder during deep lithiation because the high retention rates of 69 and 56% were measured in region C.

The delithiation limitation at 1200 mAh g^{-1} to avoid the large shrinkage of the Si/GS electrodes in region E achieved the areal capacity at 4 mAh cm^{-2} for more than 75 cycles, while the C-coated Si electrode degraded from the 17th cycle at 2.1 mAh cm^{-2} (Fig. 13). The Si/GS composite structure and the suppression of Si volume change resulted in a high delithiation capacity and good cyclability.

The Si electrode performances are summarized in Table V. Nano Si powder with few layer graphene and PBuPyMAA binder,[19] and with reduced graphene oxide[42] showed relatively high areal delithiation capacities, while the current density was low compared with the thick Si/GS electrode at 10 mAh cm^{-2}. It was also reported that the electrode structure was fragile and Li dendrites were formed for the nano Si/reduced graphene oxide electrode after 100 cycles.[42] Micro Si powder with few layer graphene[18] and with self-healing polymer[43] electrodes were cycled at much lower current densities. These results indicate that the electrical contacts in thick Si electrodes are greatly improved by the Si/GS composites. The importance of the electrical contacts for thick Si electrodes was also demonstrated by a-Si/single wall carbon nanotube electrodes, while the delithiation capacity was unstable at 8 mAh cm^{-2}.[24] Moreover, C-coated Si electrodes with Si frameworks showed the low delithiation capacities. Therefore, the wrapping structure and the stable thick GS frameworks in the Si/GS electrodes contribute to the robustness of thick Si electrodes.

Conclusions

Si electrodes for LIBs were fabricated with Si swarf treated as an industrial waste and graphite sheets from expanded graphite at a reduced cost and thermal budget. The decreases in the delithiation capacity for the electrode with Si nanopowder coated by an amorphous C layer from the 180th cycle and for thick Si electrodes were addressed by the Si/GS composites with the following processes and mechanism.

1) Si nanopowder of 60 nm∼2 μm lateral size and 9 ∼ 40 nm thickness were fabricated from Si swarf by deagglomeration with a crusher.
2) Ultrathin graphite sheets of 0.5 ∼ 13 μm lateral size and 1 ∼ 13 nm thickness were fabricated by the sonication of expanded graphite in NMP. The graphite sheets were flexible because most edges of graphite sheets were rolled.
3) Flake-shaped Si nanopowder fabricated from Si swarf was dispersed and wrapped between graphite sheets by sonication in NMP and filtering the dispersion.
4) Graphite sheets reduced the overvoltage of the Si electrode during lithiation and from the 150th cycle during delithiation, compared with an amorphous C layer. As a result, the better cyclability was achieved by the high lithiation capacity for the Si/GS electrode.
5) Ultrathin graphite sheets with flexibility closely contacted with Si nanopowder, and improved the electrical conductivity of the Si electrode compared with an amorphous C layer, resulting in the decrease in R_s. The layered Si/GS composite and bridges of ultrathin graphite sheets between the electrode islands suppressed the peeling-off, electrical isolation, fusion and crack formation in the Si/GS electrodes. These functions of the ultrathin graphite sheets retarded the increases in R_s and R_{ct} during 300 cycles.
6) Thick graphite sheets played a role of mechanically stable and conductive frameworks during 300 cycles. Wrapping Si/GS composites with thick graphite sheets secured electrolyte paths and buffer spaces for Si volume change, leading to suppression of increases in R_s and R_{ct}.
7) The Si/GS composite structure and the delithiation limitation improved the cyclability up to 901 cycles at 1200 mAh g^{-1}. The delithiation capacity and areal current density linearly increased to 4 mAh cm^{-2} and 5 mA cm^{-2}, respectively, with the mass loading for more than 75 cycles.

Table V. Comparison of electrode performances of Si electrodes.

Electrode	binder	Theoretical capacity (mAh cm^{-2})	Areal capacity (mAh cm^{-2})	Specific capacity (mAh g^{-1})	Cycle	Areal current density (mA cm^{-2})	References
nanoSi/FLG	PBuPyMAA	8.8	5.2 ∼ 4.2	1550 ∼ 1227	120	2.4	19
nanoSi/rGO	CMC	8.9	12.5 ∼ 3.9	5000 ∼ 1550	200	1.8	42
microSi/FLG	Na-PAA	7.2	3.6	1800	200	0.7	18
microSi	SHP	5.7	3.8 ∼ 2.6	1527 ∼ 1045	140	0.3	43
a-Si/SWCNT	—	8	4.2 ∼ 3.4	1900 ∼ 1540	20	5.3	24
Si/GS	CLPA, PVA	10	4[a)]	1200[a)]	>75	5	this study
Si/GS	CLPA, PVA	6	2.4[a)]	1200[a)]	>100	3	this study
Si/GS	CLPA, PVA	6	4.9 ∼ 1.6	2474 ∼ 822	100	2	this study
Si/GS	CLPA, PVA	2	1.7 ∼ 0.8	2596 ∼ 1273	300	1	this study
Si/GS	CLPA, PVA	2	0.8[a)]	1200[a)]	901	1	this study
C-coated Si	CLPA, PVA	6	4.4 ∼ 0.7	2428 ∼ 364	100	3	this study
C-coated Si	CLPA, PVA	5.7	2.1[a)]	1200[a)]	16	2.85	this study
C-coated Si	CLPA, PVA	2.1	1.6 ∼ 0.7	2386 ∼ 1114	300	1.05	this study
C-coated Si	CLPA, PVA	2.1	0.8[a)]	1200[a)]	660	1.05	this study

a) represents limited delithiation capacity. FLG: few layer graphene. rGO: reduced graphene oxide. SWCNT: single wall carbon nanotube. PBuPyMAA: poly(1-pyrenebutyl methacrylate-co-methacrylic acid). PAA: poly acryl acid. SHP: self healing polymer.

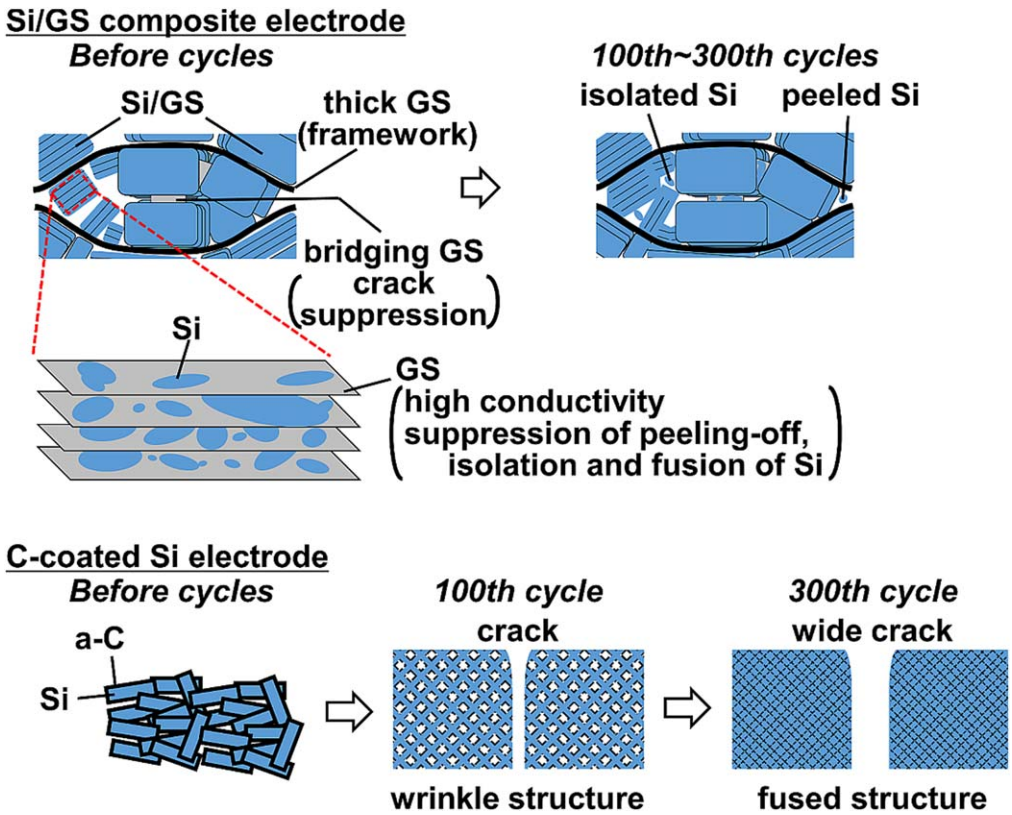

Figure 14. Schematic draw of the structures for the Si/GS and C-coated Si electrodes during cycles.

Acknowledgments

The authors acknowledge Professor H. Kobayashi for precious discussion, Y. Murakami and T. Ishibashi for TEM observation and the sample preparation, and K. Kawamura for measurement of Raman spectroscopy. This research was partly supported by JKA and its promotion funds from KEIRIN RACE, and Dynamic Alliance for Open Innovation Bridging Human, Environment and Materials, from the Ministry of Education, Culture, Sports, Science and Technology (MEXT) in Japan.

ORCID

Jaeyoung Choi https://orcid.org/0000-0001-6176-9807
Jiasheng Wang https://orcid.org/0000-0002-6133-9679
Taketoshi Matsumoto https://orcid.org/0000-0002-7430-4563

References

1. T. D. Hatchard and J. R. Dahn, *J. Electrochem. Soc.*, **151**, A838 (2004).
2. T. Gao, Q. Qu, G. Zhu, Q. Shi, F. Qian, J. Shao, and H. Zheng, *Carbon*, **110**, 249 (2016).
3. X. H. Liu, L. Zhong, S. Huang, S. X. Mao, T. Zhu, and J. Y. Huang, *ACS Nano*, **6**, 1522 (2012).
4. P. Yu, B. N. Popov, J. A. Ritter, and R. E. White, *J. Electrochem. Soc.*, **146**, 8 (1999).
5. G. A. Tritsaris, K. Zhao, O. U. Okeke, and E. Kaxiras, *J. Phys. Chem. C*, **116**, 22212 (2012).
6. K. Kimura, T. Matsumoto, H. Nishihara, T. Kasukabe, T. Kyotani, and H. Kobayashi, *J. Electrochem. Soc.*, **164**, A995 (2017).
7. T. Matsumoto, K. Kimura, H. Nishihara, T. Kasukabe, T. Kyotani, and H. Kobayashi, *J. Alloys Compd.*, **720**, 529 (2017).
8. H. Nishihara, T. Kasukabe, K. Kimura, T. Matsumoto, H. Kobayashi, and T. Kyotani, *Sci. Rep.*, **7**, 42734 (2017).
9. F. Jeschull, Y. Surace, S. Zürcher, G. Lari, M. E. Spahr, P. Novák, and S. Trabesinger, *J. Electrochem. Soc.*, **167**, 100535 (2020).
10. I. H. Son et al., *Nature Commun.*, **6**, 7393 (2015).
11. H. Kim, M. Seo, M.-H. Park, and J. Cho, *Angew. Chem. Int. Ed.*, **49**, 2146 (2010).
12. X. Li et al., *Science*, **324**, 1312 (2009).
13. C. K. Chua and M. Pumera, *Chem. Soc. Rev.*, **43**, 291 (2014).
14. S. K. Kim, H. Kim, H. Chang, B. G. Cho, J. Huang, H. Yoo, H. Kim, and H.-D. Jang, *Sci. Rep.*, **6**, 33688 (2016).
15. V. Chabota, K. Fenga, H. W. Park, F. M. Hassan, A. R. Elsayeda, A. Yu, X. Xiao, and Z. Chen, *Electrochim. Acta*, **130**, 127 (2014).
16. D. P. Wong, H.-P. Tseng, Y.-T. Chen, B.-J. Hwang, L.-C. Chen, and K.-H. Chen, *Carbon*, **63**, 397 (2013).
17. S. H. Choi, D. S. Jung, J. W. Choi, and Y. C. Kang, *Chem. Eur. J.*, **21**, 2076 (2015).
18. Q. Huang, M. J. Loveridge, R. Genieser, M. J. Lain, and R. Bhagat, *Sci. Rep.*, **8**, 1386 (2018).
19. T. Zheng, Z. Jia, N. Lin, T. Langer, S. Lux, I. Lund, A.-C. Gentschev, J. Qiao, and G. Liu, *Polymers*, **9**, 657 (2017).
20. C. Shen, X. Fang, M. Ge, A. Zhang, Y. Liu, Y. Ma, M. Mecklenburg, X. Nie, and C. Zhou, *ACS Nano*, **12**, 6280 (2018).
21. N. Liu, H. Wu, M. T. McDowell, Y. Yao, C. Wang, and Y. Cui, *Nano Lett.*, **12**, 3315 (2012).
22. X. Ding and Y. Wang, *Electrochim. Acta*, **329**, 134975 (2020).
23. H. Wu et al., *Nature Nanotech*, **7**, 310 (2012).
24. J. Yu, H. Zhan, Y. Wang, Z. Zhang, H. Chen, H. Li, Z. Zhong, and F. Su, *J. Power Sources*, **228**, 270 (2013).
25. H. Liu et al., *Appl. Surf. Sci.*, **442**, 204 (2018).
26. C. Li, C. Liu, K. Ahmed, Z. Mutlu, Y. Yan, I. Lee, M. Ozkan, and C. S. Ozkan, *RSC Adv.*, **7**, 36541 (2017).
27. U. Khan, A. O'Neill, M. Lotya, S. De, and J. N. Coleman, *Small*, **6**, 864 (2010).
28. T. Ida and H. Hibino, *J. Appl. Cryst.*, **39**, 90 (2006).
29. J. E. Smith Jr, M. H. Brodsky, B. L. Crowder, M. I. Nathan, and A. Pinczuk, *Phys. Rev. Lett.*, **26**, 642 (1971).
30. A. A. Sirenkoa, J. R. Fox, I. A. Akimov, X. X. Xia, S. Ruvimov, and Z. Liliental-Weber, *Solid State Commun.*, **113**, 553 (2000).
31. M. Nakamizo, R. Kammereck, and P. L. Walker Jr., *Carbon*, **12**, 259 (1974).
32. L. M. Malard, M. A. Pimenta, G. Dresselhaus, and M. S. Dresselhaus, *Phys. Rep.*, **473**, 51 (2009).
33. M. R. Zamfir, H. T. Nguyen, E. Moyen, Y. H. Lee, and D. Pribat, *J. Mater. Chem. A*, **1**, 9566 (2013).
34. C.-M. Wang et al., *Nano Lett.*, **13**, 758 (2013).
35. X. H. Liu et al., *Nano Lett.*, **11**, 2251 (2011).
36. J. Li and J. R. Dahn, *J. Electrochem. Soc.*, **154**, A156 (2007).
37. N. Aoki, A. Omachi, K. Uosaki, and T. Kondo, *ChemElectroChem.*, **3**, 959 (2016).
38. S. Iwamura, H. Nishihara, and T. Kyotani, *J. Power Source.*, **222**, 400 (2013).
39. T. Swamy and Y.-M. Chiang, *J. Electrochem. Soc.*, **162**, A7129 (2015).
40. Y. Domi, H. Ususi, K. Yamaguchi, S. Yodoya, and H. Sakaguchi, *ACS Appl. Mater. Interfaces*, **11**, 2950 (2019).
41. C.-Y. Chen et al., *Sci. Rep.*, **6**, 36153 (2016).
42. B. P. N. Nguyen, N. A. Kumar, J. Gaubicher, F. Duclairoir, T. Brousse, O. Crosnier, L. Dubois, G. Bidan, D. Guyomard, and B. Lestriez, *Adv. Energy Mater.*, **3**, 1351 (2013).
43. Z. Chen, C. Wang, J. Lopez, Z. Lu, Y. Cui, and Z. Bao, *Adv. Energy Mater.*, **5**, 1401826 (2015).